

# Robust Autocalibrated Structured Low-Rank EPI Ghost Correction

Rodrigo A. Lobos<sup>1,2</sup>, W. Scott Hoge<sup>4,5</sup>, Ahsan Javed<sup>1,2</sup>, Congyu Liao<sup>5,6</sup>, Kawin Setsompop<sup>5,6</sup>, Krishna S. Nayak<sup>1,2,3</sup>, Justin P. Haldar<sup>1,2,3</sup>

<sup>1</sup>Ming Hsieh Department of Electrical and Computer Engineering, University of Southern California, Los Angeles, CA, USA

<sup>2</sup> Signal and Image Processing Institute, University of Southern California, Los Angeles, CA, USA

<sup>3</sup>Department of Biomedical Engineering, University of Southern California, Los Angeles, CA, USA

<sup>4</sup>Department of Radiology, Brigham and Women's Hospital, Boston, MA, USA

<sup>5</sup>Department of Radiology, Harvard Medical School, Boston, MA, USA

<sup>6</sup> Athinoula A. Martinos Center for Biomedical Imaging, Charlestown, MA, USA

## Address Correspondence to:

Rodrigo A. Lobos  
University of Southern California  
University Park Campus, 3710 McClintock Avenue, Ronald Tutor Hall (RTH) #317,  
Los Angeles, CA 90036.  
Tel: (+1)323-561-2265  
Email: rlobos@usc.edu

Submitted to Magnetic Resonance in Medicine

MANUSCRIPT BODY APPROXIMATE WORD COUNT = 5000

# ABSTRACT

**Purpose:** We propose and evaluate a new structured low-rank method for EPI ghost correction called Robust Autocalibrated LORAKS (RAC-LORAKS). The method can be used to suppress EPI ghosts arising from the differences between different readout gradient polarities and/or the differences between different shots. It does not require conventional EPI navigator signals, and is robust to imperfect autocalibration data.

**Methods:** Autocalibrated LORAKS is a previous structured low-rank method for EPI ghost correction that uses GRAPPA-type autocalibration data to enable high-quality ghost correction. This method works well when the autocalibration data is pristine, but performance degrades substantially when the autocalibration information is imperfect. RAC-LORAKS generalizes Autocalibrated LORAKS in two ways. First, it does not completely trust the information from autocalibration data, and instead considers the autocalibration and EPI data simultaneously when estimating low-rank matrix structure. And second, it uses complementary information from the autocalibration data to improve EPI reconstruction in a multi-contrast joint reconstruction framework. RAC-LORAKS is evaluated using simulations and in vivo data, and compared to state-of-the-art methods.

**Results:** RAC-LORAKS is demonstrated to have good ghost elimination performance compared to state-of-the-art methods in several complicated acquisition scenarios (including gradient-echo brain imaging, diffusion-encoded brain imaging, and cardiac imaging).

**Conclusion:** RAC-LORAKS provides effective suppression of EPI ghosts and is robust to imperfect autocalibration data.

# KEYWORDS

Echo-planar imaging; Nyquist ghost correction; structured low-rank matrix recovery; constrained reconstruction; multi-contrast reconstruction.

# 1 INTRODUCTION

Echo-planar imaging (EPI) is a widely-used high-speed MRI acquisition strategy (1), but is subject to several undesirable artifacts (2). Nyquist ghosts are one of the most common EPI artifacts, and occur because of systematic differences between the interleaved lines of k-space that are acquired with different readout gradient polarities, and/or because of systematic differences between interleaved lines of k-space data that are acquired with different shots in a multi-shot acquisition. Despite substantial efforts over several decades to solve this problem (2–20), the widely-deployed modern ghost correction schemes are still prone to incomplete ghost suppression, as illustrated in Supporting Information Fig. S1.

Recently, structured low-rank matrix methods for ghost correction (16–20) have received increasing attention for their ability to provide excellent ghost-suppression performance without the need for additional “navigator” information (i.e., reference scans collected alongside each EPI readout that allow estimation of the systematic inconsistencies between different gradient polarities or different shots). These methods can suppress ghosts better than navigator-based methods, and eliminate the need to acquire navigators for each EPI readout. Among different structured low-rank matrix approaches, a ghost correction method based on Autocalibrated LORAKS (AC-LORAKS) (21) was previously demonstrated to yield high-quality results across a range of different scenarios (18). To eliminate a fundamental ambiguity in structured low-rank matrix recovery from uniformly undersampled EPI data (18), AC-LORAKS makes use of parallel imaging subspace information estimated from autocalibration (ACS) data acquired in a pre-scan. This ACS-based approach is similar to standard autocalibrated parallel imaging methods like GRAPPA (22), SPIRiT (23), and PRUNO (24).

While the AC-LORAKS approach to ghost correction generally works well when the ACS data is pristine and well-matched to the EPI data to be reconstructed, there are many situations where experimental conditions (e.g., subject motion, eddy currents, etc.) can lead to artifacts within the ACS data or mismatches between the ACS and EPI data. The performance of the AC-LORAKS ghost correction procedure degrades in the presence of these ACS artifacts and mismatches. This problem with imperfect ACS data could be

especially troublesome in contexts where the prescan would be done once before acquiring a long sequence of multiple EPI images (e.g., in BOLD fMRI or diffusion MRI applications), and then used to reconstruct each image in the sequence.

In this paper, we propose an extension of AC-LORAKS for EPI ghost correction that is more robust to imperfections in the ACS data. The new method, called Robust Autocalibrated LORAKS (RAC-LORAKS), has two major differences from the previous AC-LORAKS approach. First, RAC-LORAKS does not completely trust the subspace information learned from the ACS data, but rather uses a formulation that balances the information from the ACS data with information from the EPI data being reconstructed. And second, RAC-LORAKS uses the ACS data to provide additional complementary information for the reconstruction of the EPI data within a multi-contrast joint reconstruction framework (25). Preliminary accounts of the first strategy were previously reported in recent conferences (26, 27), although we have not previously reported the combination with the second strategy.

## 2 THEORY

For simplicity, our description of EPI ghost correction will generally assume that we are correcting ghosts associated with the differences between data acquired with different readout gradient polarities in a single-shot EPI experiment. However, since the ghost model for bipolar gradients is nearly identical to the ghost model for multi-shot acquisition, the same approach is easily adapted *mutatis mutandis* to multi-shot acquisition with an arbitrary number of shots (18).

### 2.1 Background: Structured Low-Rank EPI ghost correction

Structured low-rank matrix methods for EPI ghost correction (16–20) can be viewed as an extension of structured low-rank matrix methods for conventional MR image reconstruction (24, 28–34), and are based on the same underlying theoretical principles. In particular, it has been shown that when MRI images have limited support, smooth phase variations, multi-channel correlations, or transform-domain sparsity, then the MRI k-space data will be

linearly predictable (35), which means that convolutional Hankel- or Toeplitz-structured matrices formed from the k-space data will possess low-rank characteristics. This observation means that MRI reconstruction can be reformulated as structured low-rank matrix recovery. Importantly, these structured low-rank matrix recovery methods can even be successful in calibrationless scenarios where ACS data or other prior information about the spatial support, phase, or multi-channel sensitivity profiles is not available (30–32).

Structured low-rank EPI ghost correction methods combine these principles with the earlier observation that EPI data acquired from different gradient polarities or different shots can be treated as coming from different effective “channels” in a parallel imaging experiment, where the systematic differences between different polarities or shots lead to different phase or magnitude modulations of the underlying EPI image (9, 11, 12, 15). Since structured low-rank methods for conventional image reconstruction automatically account for the unknown sensitivity maps that modulate the underlying image in a parallel imaging experiment, it is reasonable to apply these same types of methods to handle the unknown polarity- or shot-dependent modulations that manifest in EPI ghost correction.

For the sake of brevity, we will focus the remainder of our review on the AC-LORAKS method for EPI ghost correction (18), since our proposed RAC-LORAKS method is a generalization of AC-LORAKS. The AC-LORAKS method for EPI ghost correction is based on solving the following regularized optimization problem subject to exact data consistency constraints:

$$\left\{ \hat{\mathbf{k}}^+, \hat{\mathbf{k}}^- \right\} = \arg \min_{\{\mathbf{k}^+, \mathbf{k}^-\}} \left\| \mathcal{P}_C(\mathbf{k}^+) \mathbf{N} \right\|_F^2 + \left\| \mathcal{P}_C(\mathbf{k}^-) \mathbf{N} \right\|_F^2 + \lambda J_r([\mathcal{P}_S(\mathbf{k}^+) \mathcal{P}_S(\mathbf{k}^-)]). \quad [1]$$

In this expression,  $\mathbf{k}^+$  and  $\mathbf{k}^-$  respectively represent the ideal fully-sampled multi-channel Cartesian k-space data for the positive and negative readout gradient polarities;  $\mathcal{P}_C(\cdot)$  is the LORAKS operator that maps the k-space data into a structured matrix that should possess low-rank if the multi-channel image possess limited support and/or interchannel parallel imaging correlations (31, 32);  $\mathcal{P}_S(\cdot)$  is the LORAKS operator that maps the k-space data into a structured matrix that should possess low-rank if the multi-channel image possess limited support, smooth phase, and/or interchannel parallel imaging correlations (31, 32);

the matrix  $\mathbf{N}$  comprises an orthonormal (i.e.,  $\mathbf{N}^H \mathbf{N} = \mathbf{I}$ ) basis for the nullspace of the matrix  $\begin{bmatrix} \mathcal{P}_C(\mathbf{k}_{\text{acs}}^+) \\ \mathcal{P}_C(\mathbf{k}_{\text{acs}}^-) \end{bmatrix}$ , where  $\mathbf{k}_{\text{acs}}^+$  and  $\mathbf{k}_{\text{acs}}^-$  respectively represent the ACS data for the positive and negative readout gradient polarities;  $\lambda$  is a regularization parameter;  $J_r(\cdot)$  is a regularization penalty that promotes low-rank characteristics; and  $\|\cdot\|_F$  denotes the Frobenius norm. There are theoretical benefits to choosing a nonconvex low-rank regularization penalty (18), and the previous AC-LORAKS approach for ghost correction (18) used the nonconvex function proposed in the original LORAKS paper (31) defined by

$$J_r(\mathbf{X}) = \min_{\mathbf{Y}} \|\mathbf{X} - \mathbf{Y}\|_F^2 \text{ s.t. } \text{rank}(\mathbf{Y}) \leq r, \quad [2]$$

where  $r$  is a user-selected rank parameter. This regularization penalty encourages the reconstructed matrix to be well-approximated (in a least-squares sense) by a matrix of rank- $r$  or lower.

The first two terms appearing on the right hand side of Eq. [1] respectively impose limited support and parallel imaging constraints on the reconstructions of the positive and negative readout gradient polarities. The constraints that are used in these terms are captured by the nullspace matrix  $\mathbf{N}$ , which is learned in advance from the ACS data. As a result, there is an implicit assumption that the support and parallel imaging constraints that were valid for the ACS data are also valid for the EPI data to be reconstructed. Note that if the third term were removed from Eq. [1], then these first two terms would reduce to performing separate PRUNO (24) or conventional AC-LORAKS (21) reconstructions of the data from each polarity. Using ACS data can be important in this context, since it has been theoretically proven that support and parallel imaging information cannot be extracted unambiguously from undersampled EPI data alone (18). While other options exist for removing ambiguity (e.g., using SENSE-like (36) image-domain constraints (17, 18)), it was previously observed that the AC-LORAKS approach (i.e., using GRAPPA-like (22) Fourier-domain constraints) offered better performance (18).

The third term of Eq. [1] couples the reconstruction of the two polarities together, allowing the reconstruction of one polarity to benefit from information from the other polarity, while also introducing phase constraints to allow the reconstruction to benefit from k-space

conjugate symmetry characteristics. In particular, the third term implicitly and automatically imposes the following constraints whenever they are compatible with the measured data: limited image support, smooth phase, interchannel parallel imaging correlations, and interpolarity correlations. Notably, these constraints are all imposed implicitly through the nullspace of a structured matrix, and if a given constraint is not compatible with the measured data, then that constraint will automatically not be imposed by the reconstruction procedure (35).

The ACS data for AC-LORAKS ghost correction has typically been acquired using the same process used by Dual Polarity GRAPPA (DPG) (11). In particular, assuming a parallel imaging acceleration factor of  $R$ , DPG employs a  $2R$ -shot EPI prescan. The data from different shots and different gradient polarities is then rearranged and interleaved to form one fully-sampled ACS dataset comprised only of data acquired with a positive readout gradient polarity ( $\mathbf{k}_{\text{acs}}^+$ ) and another fully-sampled ACS dataset comprised only of data acquired with a negative readout gradient polarity ( $\mathbf{k}_{\text{acs}}^-$ ). Since this ACS acquisition strategy is based on a multi-shot approach, it therefore may be prone to ghosting artifacts due to shot-to-shot variations. In addition, since the ACS data is often acquired only once at the beginning of a long multi-image EPI scan (e.g., in BOLD fMRI or diffusion MRI experiments), the ACS data acquired at the beginning of the experiment may gradually become mismatched with data acquired at later time points due to scanner drift, subject motion, etc. As noted previously, the ghost correction performance of AC-LORAKS can be substantially degraded when there are mismatches between the ACS data and the EPI data to be reconstructed.

## 2.2 RAC-LORAKS

Our proposed RAC-LORAKS method is based on solving the following optimization problem

$$\begin{aligned} \left\{ \hat{\mathbf{k}}^+, \hat{\mathbf{k}}^-, \hat{\mathbf{N}} \right\} = \arg \min_{\{\mathbf{k}^+, \mathbf{k}^-, \mathbf{N}\}} & \left\| \mathcal{P}_C(\mathbf{k}^+) \mathbf{N} \right\|_F^2 + \left\| \mathcal{P}_C(\mathbf{k}^-) \mathbf{N} \right\|_F^2 \\ & + \eta \left\| \mathcal{P}_C(\mathbf{k}_{\text{acs}}^+) \mathbf{N} \right\|_F^2 + \eta \left\| \mathcal{P}_C(\mathbf{k}_{\text{acs}}^-) \mathbf{N} \right\|_F^2 \\ & + \lambda J_r \left( \begin{bmatrix} \mathcal{P}_S(\mathbf{k}^+) & \mathcal{P}_S(\mathbf{k}^-) & \mathcal{P}_S(\mathbf{k}_{\text{acs}}^+) & \mathcal{P}_S(\mathbf{k}_{\text{acs}}^-) \end{bmatrix} \right) \end{aligned} \quad [3]$$

subject to exact data consistency constraints on  $\mathbf{k}^+$  and  $\mathbf{k}^-$  and subject to orthonormality constraints on  $\mathbf{N}$  such that  $\mathbf{N}^H \mathbf{N} = \mathbf{I}$ . This optimization problem involves four user-selected parameters: the regularization parameters  $\eta$  and  $\lambda$ , the rank parameter  $r$ , and the number of columns  $p$  of the matrix  $\mathbf{N}$  (which determines the dimension of the approximate nullspace).

Equation [3] has two main differences from Eq. [1]. First, instead of choosing a predetermined value of the approximate nullspace matrix  $\mathbf{N}$  that depends only on the ACS data,  $\mathbf{N}$  is now an optimization variable that depends on both the ACS data and the EPI data to be reconstructed. This allows the reconstruction to be more robust against possible imperfections in the ACS data. The extent to which the ACS data is trusted is controlled by the user-selected parameter  $\eta$ . In the limit as  $\eta \rightarrow \infty$ , the approximate nullspace matrix  $\mathbf{N}$  will converge to the fixed matrix from Eq. [1].

The second difference is that the final term of Eq. [3] now includes structured matrices formed from the ACS data, in addition to the previous structured matrices formed from the EPI data to be reconstructed. By concatenating the ACS data in this way, we are essentially treating the ACS data in the same way that we would treat additional channels in a parallel imaging experiment. Although the ACS data may not have the same contrast as the EPI data to be reconstructed, it has previously been shown that treating multi-contrast information like additional channels in a parallel imaging experiment often leads to improved reconstruction performance (25). While this improvement has been justified empirically, some level of theoretical justification for this approach can be obtained by modeling different image contrasts as different modulations of some latent image (35).

Algorithmically, Eq. [3] can be minimized using existing algorithms for LORAKS optimization (18, 31, 32, 37). In particular, it is not hard to show that the solution to Eq. [3] can be equivalently obtained by solving:

$$\{\hat{\mathbf{k}}^+, \hat{\mathbf{k}}^-\} = \arg \min_{\{\mathbf{k}^+, \mathbf{k}^-\}} J_{(C-p)} \left( \begin{bmatrix} \mathcal{P}_C(\mathbf{k}^+) \\ \mathcal{P}_C(\mathbf{k}^-) \\ \sqrt{\eta} \mathcal{P}_C(\mathbf{k}_{\text{acs}}^+) \\ \sqrt{\eta} \mathcal{P}_C(\mathbf{k}_{\text{acs}}^-) \end{bmatrix} \right) + \lambda J_r \left( \begin{bmatrix} \mathcal{P}_S(\mathbf{k}^+) & \mathcal{P}_S(\mathbf{k}^-) & \mathcal{P}_S(\mathbf{k}_{\text{acs}}^+) & \mathcal{P}_S(\mathbf{k}_{\text{acs}}^-) \end{bmatrix} \right),$$

[4]

where  $J_{(C-p)}(\cdot)$  is the same as  $J_r(\cdot)$  but replacing the rank parameter  $r$  with the rank parameter  $(C - p)$ , where  $C$  is the number of columns of the LORAKS matrix formed by  $\mathcal{P}_C(\cdot)$ . Equation [4] is convenient because it takes the same form as previous LORAKS optimization problems involving multiple  $J_r(\cdot)$  terms (31). For this paper, we use a multiplicative half-quadratic majorize-minimize algorithm to minimize this objective function (37), which takes advantage of FFT-based matrix multiplications to improve computational complexity (38).

The RAC-LORAKS solution is obtained through the optimization of a nonconvex cost function. As such, the algorithm has the potential to converge to an undesirable local minimum. For the results shown in this paper, we initialize RAC-LORAKS using the output of DPG, which is a naive initialization with minimal processing cost. Other choices could potentially result in even higher performance, but are not considered here.

## 3 METHODS

### 3.1 Datasets used for Evaluation

As described below, we evaluated the characteristics of RAC-LORAKS using data from several different contexts.

#### 3.1.1 Gradient-Echo Brain data

In one set of experiments, we acquired *in vivo* human brain data using a gradient-echo EPI sequence with parameters that are somewhat similar to a BOLD fMRI experiment. Data was acquired on a Siemens 3T Prisma Fit scanner using a standard 32-channel receiver array. The data was acquired using  $\text{FOV} = 220 \text{ mm} \times 220 \text{ mm}$ ; matrix size =  $128 \times 128$ ; slice thickness = 3 mm; and  $\text{TR} = 2 \text{ sec}$ . In one subject, data was acquired without acceleration ( $R = 1$ ) with  $\text{TE} = 47 \text{ msec}$ . From this same subject, data was also acquired for parallel imaging acceleration factors of  $R = 2, 3, 4$  with  $\text{TE} = 35 \text{ msec}$ . In a second subject, data was acquired for parallel imaging acceleration factors of  $R = 5, 6$  with  $\text{TE} = 35 \text{ msec}$ . In all cases, fully-sampled ACS data was acquired using the same interleaved  $2R$ -shot EPI prescan

as used for DPG (11).

Each dataset was acquired with two different slice orientations. In one case, we acquired data with a conventional axial slice orientation. However, because Nyquist ghost problems tend to be more extreme with oblique acquisitions due to concomitant fields that can produce substantial nonlinear 2D phase differences between positive and negative readout polarities (10, 11, 39–41), we also acquired data with a double-oblique slice orientation to test performance in a more challenging scenario. For this case the data was acquired with  $TR = 2.08$  sec and  $TE = 35$  msec for each parallel imaging acceleration factor.

### 3.1.2 Diffusion-encoded Brain Data

In another set of experiments, we acquired *in vivo* human brain data using a diffusion-encoded spin-echo EPI sequence. Data was acquired on a Siemens 3T Prisma Fit scanner using a standard 32-channel receiver array. For the sake of computational complexity, this data was subsequently reduced to 16 channels using standard coil-compression techniques. The data was acquired using  $FOV = 220 \text{ mm} \times 220 \text{ mm}$ ; matrix size =  $220 \times 220$ ; slice thickness = 5 mm;  $TR = 2.8$  sec;  $TE = 63$  msec;  $b$ -values of 0 sec/mm<sup>2</sup> and 1000 sec/mm<sup>2</sup>; 6 diffusion encoding directions; parallel imaging acceleration factor  $R = 3$ ; and 6/8ths partial Fourier sampling. ACS data was acquired using the same interleaved  $2R$ -shot EPI prescan as used for DPG (11), except that the data was acquired with lower resolution along the phase encoding dimension (i.e., we only acquired 45 phase-encoding lines for the ACS data). Due to the random phase variations associated with diffusion encoding gradients, the ACS data was acquired without diffusion weighting.

### 3.1.3 Cardiac Data

In a third set of experiments, we acquired *in vivo* human cardiac data during diastole using a spin-echo EPI sequence with parameters that are typical for a myocardial arterial spin labeling experiment (42). Data was acquired on a GE 3T Signa HDx scanner with an 8-channel cardiac coil. The data was acquired using  $FOV = 280 \text{ mm} \times 140 \text{ mm}$ ; matrix size =  $128 \times 64$ ; slice thickness = 10 mm;  $TR = 55$  msec;  $TE = 32.9$  msec; velocity cutoff = 5 cm/s; no parallel imaging acceleration ( $R = 1$ ); and 5/8ths partial Fourier sampling. ACS

data was acquired using the same interleaved  $2R$ -shot EPI prescan as used for DPG (11), but with  $5/8$ ths partial Fourier sampling. Data was acquired with a double-oblique slice orientation to achieve a mid-short axis view.

### 3.2 Simulations

In addition to in vivo data, the different methods were also evaluated using simulations where a gold standard was present. For these simulations, we took two in vivo gradient-echo brain datasets with axial slice orientation and  $R = 2$  from the same scan session, and reconstructed them both using AC-LORAKS. This provides two sets of fully-sampled ghost-free images. One of these sets was used for ACS data, while the other was undersampled (including parallel imaging acceleration, along with interleaving the data from positive and negative gradient polarities) to simulate EPI data. These datasets were acquired roughly 5 minutes apart, allowing time for mismatches to evolve. Since ghost correction is frequently more difficult for EPI datasets with 2D nonlinear phase differences between the two polarities, we applied an additional 2D nonlinear phase pattern to make the problem more challenging. We also used slightly different phase differences for the EPI dataset and the ACS dataset to mimic the situation where the ACS data does not provide accurate phase or phase-difference information about the EPI data. To mimic the situation where image magnitude characteristics are also different between the ACS data and EPI data, we added a Gaussian-shaped additive image hyperintensity to the EPI data that we did not add to the ACS data. The fully-sampled ACS and EPI datasets used for simulation are illustrated in Supporting Information Fig. S2.

Simulations were performed based on conventional multi-channel data, and we also performed a simulation in a very challenging single-channel setting. For this, single-channel data was obtained by a linear combination of the multi-channel data (43), and the images used for this case are also shown in Supporting Information Fig. S2. Single-channel ghost correction is a difficult setting where only a few previous methods have had any success (16, 18). This case is hard because even with unaccelerated data ( $R = 1$ ), each polarity has an effective acceleration factor of  $R = 2$  when the data for each readout gradient polarity is separated, and it can be difficult to reconstruct  $R = 2$  data without multi-channel information.

### 3.3 Data Processing

RAC-LORAKS was applied to perform reconstruction and ghost correction on these datasets. For comparison against existing methods, the datasets were also reconstructed using the previous AC-LORAKS ghost-correction method (18), DPG (11), and MUSSELS (17).

For some of the datasets we consider, the ACS data may be incomplete due to low-resolution ACS acquisition (i.e., the brain diffusion data) or partial Fourier ACS acquisition (i.e., the cardiac data). In such cases, we modify RAC-LORAKS to consider the fully sampled ACS data vectors  $\mathbf{k}_{\text{acs}}^+$  and  $\mathbf{k}_{\text{acs}}^-$  as additional variables to be optimized in Eq. [4], subject to ACS data consistency constraints.

For RAC-LORAKS and AC-LORAKS, the regularization parameters  $\lambda$  and  $\eta$  were selected manually based on subjective visual inspection reconstruction quality and ghost-reduction performance for in vivo data, and to minimize quantitative error measures for simulated data. The rank-related parameters  $p$  and  $r$  were selected based on the singular value characteristics of LORAKS matrices formed from the ACS data. The rank parameters were set based on the points at which the singular value curves begin to flatten out, which is a common rank estimation technique for noisy matrices.

DPG is a ghost correction method that treats different gradient polarities like different coils in a parallel imaging experiment, and uses a dual GRAPPA kernel estimated from ACS data for image reconstruction (11). To facilitate the comparison between DPG and RAC-LORAKS, we have adapted DPG to output two sets of images, one for  $\mathbf{k}^+$  and one for  $\mathbf{k}^-$ , rather than the original DPG implementation that fuses information from the two polarities together into a single output.

MUSSELS is a structured low-rank matrix recovery method that uses SENSE-type parallel imaging constraints together with nuclear norm regularization to impose low-rank constraints (17). While MUSSELS was originally developed for multi-shot EPI ghost correction, it can apply equally well to the ghost correction problem associated with different gradient polarities. Sensitivity maps for MUSSELS were estimated by applying ESPIRiT (29) to the same ACS data used for the other methods. The regularization parameter for MUSSELS was selected manually based on subjective visual inspection of reconstruction quality and

ghost-reduction performance in the case of in vivo data, or to minimize quantitative error measures for simulated data.

Note that DPG and MUSSELS were both developed for the multi-channel setting. We can adapt DPG to the single-channel setting in straightforward ways (18), and we apply this adaptation to the single-channel simulated data. We did not adapt MUSSELS to the single-channel case. Note that the SENSE-based constraints used by MUSSELS would reduce to a simple spatial-domain support constraint in the single-channel case, which is not strong enough to yield good performance results.

For all methods, results were visualized by using a standard square-root sum-of-squares technique to combine the images from different coils and different gradient polarities into a single image. Results from in vivo experiments were evaluated qualitatively, since a gold standard reference was not available in these cases.

Simulation results were evaluated quantitatively using the normalized root mean-squared error (NRMSE):

$$\text{NRMSE} \triangleq \frac{\sqrt{\|\hat{\mathbf{k}}^+ - \mathbf{k}_{\text{gold}}^+\|_2^2 + \|\hat{\mathbf{k}}^- - \mathbf{k}_{\text{gold}}^-\|_2^2}}{\sqrt{\|\mathbf{k}_{\text{gold}}^+\|_2^2 + \|\mathbf{k}_{\text{gold}}^-\|_2^2}}, \quad [5]$$

where  $\mathbf{k}_{\text{gold}}^+$  and  $\mathbf{k}_{\text{gold}}^-$  are respectively the gold standard values for the positive and negative gradient polarities. We also plotted Fourier Error Spectrum Plots (ESPs) to gain further insight into how the errors were distributed across different spatial resolutions scales (44). An ESP is designed to reveal the spectral characteristics of the error, and for example, can discriminate between methods that make more errors in the low-resolution features of an image versus methods that make more errors in high-resolution features.

## 4 RESULTS

Figure 1 shows ACS data and reconstruction results from the in vivo gradient-echo brain data with an axial slice orientation. The ACS data in this case does not have strong artifacts, although close inspection does reveal that ACS ghost artifacts are present. As can be seen, all ghost correction methods work well at smaller acceleration factors, although

performance begins to degrade at larger acceleration factors. We observe that, compared to other methods, the visual quality of the MUSSELS reconstruction seems to degrade most rapidly as a function of acceleration factor. The DPG method had qualitatively better performance than MUSSELS in this case. However, a close inspection of the images reveals that the DPG results are not entirely ghost-free even for the unaccelerated ( $R = 1$ ) case. This may be expected since ghosts are present in the ACS data, and DPG attempts to match the ACS characteristics. In spite of the ACS artifacts, the AC-LORAKS reconstruction still has good performance at low acceleration factors, although exhibits substantial degradation in image quality at the highest acceleration factors. However, the RAC-LORAKS reconstruction appears to have much higher quality than the other methods, even at very high acceleration factors like  $R = 6$ . (Note that when  $R = 6$ , the effective acceleration factor is  $R = 12$  when each readout gradient polarity is considered separately. This leads to a highly ill-posed inverse problem).

To further illustrate the characteristics of these datasets, we also computed temporal signal-to-noise ratio (tSNR) maps (the ratio between the temporal mean and the temporal standard deviation across 20 time points) for DPG and RAC-LORAKS with the  $R = 2$  data. These maps are shown in Fig. 2. As can be seen, RAC-LORAKS has higher tSNR within the brain than DPG, as well as demonstrating substantially less-prominent ghosting structure in the image background.

Figure 3 shows results from the *in vivo* gradient-echo brain data with a double-oblique slice orientation. This case is more challenging than the previous one due to the complicated nonlinear 2D spatial phase differences we observed between data acquired with positive and negative polarities (as visualized in the figure), as well as the more substantial ghosting artifacts present in the ACS data. Despite the more extreme scenario, the different ghost reconstruction methods have similar characteristics to those observed in the previous case, with RAC-LORAKS appearing to demonstrate the cleanest overall results.

Figure 4 shows reconstruction results from the multi-channel simulation, with quantitative NRMSE values reported in Table 1 and corresponding ESPs shown in Fig. 5. Qualitatively, the results from Fig. 4 have similar characteristics to the results observed with *in vivo* data. Notably, RAC-LORAKS is able to consistently reconstruct a high-quality im-

age that bears close resemblance to the gold standard image, while methods like DPG and AC-LORAKS have artifacts due to the small mismatches between the ACS and EPI data. The visual assessment of reconstruction quality matches well with the quantitative NRMSE assessment shown in Table 1. Although AC-LORAKS has slightly smaller NRMSE values than RAC-LORAKS at lower parallel imaging acceleration factors, both methods perform comparably well in this range, and RAC-LORAKS has the best performance at high acceleration factors. It should also be pointed out that for  $R = 5$  DPG and RAC-LORAKS have similar quantitative results. However, closer inspection of the images in Fig. 4 reveals that DPG has an obvious unresolved aliasing artifact associated with the Gaussian-shaped hyperintensity that was present in the EPI data but not in the ACS data. The ESP plots in Fig. 5 enable a more nuanced analysis. These results suggest that RAC-LORAKS has good performance at all spatial frequencies, meaning that it is good at reconstructing image features across the whole range of resolution scales.

Figure 6 shows reconstruction results from the single-channel simulation, with quantitative NRMSE values reported in Supporting Information Table S1. While DPG and AC-LORAKS can be reasonably successful for single-channel data with  $R = 1$  when the ACS data is pristine (18), these results demonstrate that this performance can be sensitive to the quality of the ACS data. In contrast, RAC-LORAKS is substantially more successful for  $R = 1$ . Notably, RAC-LORAKS also performed well for the even more challenging  $R = 2$  case, unlike the other methods. For reference, note that even with high-quality ACS data, the previous AC-LORAKS method did not yield good results with similar single-channel  $R = 2$  data (18).

Figure 7 shows reconstruction results from the *in vivo* diffusion brain data, while Fig. 8 shows the same results with  $10\times$  intensity amplification to highlight the ghost characteristics. As can be seen, the ACS data has ghost artifacts in all cases, and both MUSSELS and DPG reconstructions also exhibit unsuppressed ghosting artifacts. On the other hand, both AC-LORAKS and RAC-LORAKS are relatively ghost-free in this example and have only minor differences from one another. (It might be argued that the RAC-LORAKS result has a slightly less-noisy appearance than the AC-LORAKS result, but if so, this difference is very subtle). While this result does not demonstrate an obvious advantage for RAC-LORAKS

over AC-LORAKS, it should be observed that this diffusion result is at least consistent with the previous gradient-echo results, in which we also did not observe a substantial difference between RAC-LORAKS and AC-LORAKS when  $R = 3$ . In addition, this case involves a very substantial contrast difference between the ACS data and the EPI data. This difference does not appear to have adversely affected the performance characteristics of these methods in substantial ways.

Finally, Fig. 9 shows results from the in vivo cardiac data. While this data was not accelerated ( $R = 1$ ), this case is challenging because of the double-oblique slice orientation as well as the substantial artifacts present in the ACS data resulting from cardiac motion-induced shot-to-shot variations. In addition, this case can also be challenging for SENSE-based methods (like MUSSELS), due to the use of a small FOV with aliasing. When aliasing is present within the FOV, it violates the standard SENSE modeling assumption of one sensitivity map value per spatial location, which generally leads to artifacts if not properly accounted for. The results demonstrate that both MUSSELS and DPG have substantial residual ghosting artifacts, which might not be surprising given the high degree of corruption that is present in the ACS data. On the other hand, both AC-LORAKS and RAC-LORAKS are more successful at suppressing the ghosts. Without a gold standard reference, it is hard to establish definitively whether AC-LORAKS or RAC-LORAKS is better in this example, although we believe that the RAC-LORAKS result demonstrates slightly less ghosting than AC-LORAKS, particularly on the left side of the image where the ACS data and DPG both have particularly strong ghost artifacts.

## 5 DISCUSSION

The results in the previous section demonstrated that, in the presence of imperfect ACS data, RAC-LORAKS frequently offers similar or better performance to the previous AC-LORAKS ghost correction method that it generalizes, while both of these methods perform substantially better than methods like MUSSELS or DPG. We also observed that RAC-LORAKS appears to have the biggest advantage over AC-LORAKS in scenarios where the parallel imaging acceleration factor was high. However, it should be noted that RAC-LORAKS has

one additional regularization parameter than AC-LORAKS (i.e.,  $\eta$ , which controls the level of trust placed in the information from the ACS data). In our experience, manual tuning of this parameter is not hard (i.e., we always started from the small value  $\eta = 10^{-3}$ , and frequently did not have to modify this value to achieve satisfying results). However, the method would be easier to use if the selection of  $\eta$  could be automated. We believe this is an interesting topic for future work.

While RAC-LORAKS offers good performance, the reconstruction can also be more computationally expensive than existing methods. For example, for the results shown with  $R = 1$  in Fig. 1, RAC-LORAKS used  $\approx 45$  min of reconstruction time, while MUSSELS, DPG, and AC-LORAKS respectively used  $\approx 15$  min,  $\approx 2$  min, and  $\approx 100$  min. All methods were implemented in MATLAB on a standard desktop computer with an Intel Xeon E5-1603 2.8 GHz quad core CPU processor and 32GB of RAM. While this long relatively long computation time may be a concern, it should be noted that we are reporting the results of a simple proof-of-principle implementation, and we did not spend much time to optimize the computational efficiency of this approach. We believe that major improvements may be possible by leveraging better computational hardware, smarter algorithms, and more efficient implementations. However, RAC-LORAKS is notably faster than AC-LORAKS, and it appears that this speed difference results from the fact that RAC-LORAKS has consistently faster convergence than AC-LORAKS in this setting. The reason for this faster convergence is unclear at this stage, although we believe that a detailed analysis of convergence characteristics is beyond the scope of the present paper.

While this paper focused on EPI ghost correction for standard single-slice excitation, we believe that the extension of these ideas to simultaneous multi-slice EPI acquisitions (similar to Refs. (19, 20, 45, 46)) is a very promising research direction.

Finally, the techniques developed in this work may apply more broadly than just EPI settings. Specifically, we believe that the basic principles employed by RAC-LORAKS (i.e., not completely trusting the accuracy of ACS data and leveraging ACS data to provide additional information in a multi-contrast framework) could be applied broadly to settings where ACS data may be imperfect and the image reconstruction problem may be highly ill-posed.

## 6 CONCLUSIONS

This work proposed and evaluated RAC-LORAKS, a new structured low-rank matrix method for EPI ghost correction. RAC-LORAKS uses ACS data and k-space domain linear predictive modeling to stabilize the solution of the ill-posed inverse problem, and was observed to offer advantages relative to state-of-the-art ghost correction methods like AC-LORAKS, DPG, and MUSSELS.

## ACKNOWLEDGMENTS

This work was supported in part by NSF CAREER award CCF-1350563 and NIH grants R01-MH116173, R21-EB022951, R01-NS089212, R01-NS074980, and NIH R01-HL130494. Computation for some of the work described in this paper was supported by the University of Southern California’s Center for High-Performance Computing (<http://hpcc.usc.edu/>).

## References

1. Stelhing MK, Turner R, Mansfield P. Echo-planar imaging: Magnetic resonance imaging in a fraction of a second. *Science* 1991;254:43–50.
2. Bernstein MA, King KF, Zhou XJ. *Handbook of MRI Pulse Sequences*. Burlington: Elsevier Academic Press. 2004.
3. Bruder H, Fischer H, Reinfelder HE, Schmitt F. Image reconstruction for echo planar imaging with nonequidistant k-space sampling. *Magn Reson Med* 1992;23:311–323.
4. Hu X, Le TH. Artifact reduction in EPI with phase-encoded reference scan. *Magn Reson Med* 1996;36:166–171.
5. Buonocore MH, Gao L. Ghost artifact reduction for echo planar imaging using image phase correction. *Magn Reson Med* 1997;38:89–100.
6. Chen Nk, Wyrwicz AM. Removal of EPI Nyquist ghost artifacts with two-dimensional phase correction. *Magn Reson Med* 2004;51:1247–1253.

7. Skare S, Clayton D, Newbould R, Moseley M, Bammer R. A fast and robust minimum entropy based non-interactive Nyquist ghost correction algorithm. In: *Proc. Int. Soc. Magn. Reson. Med.*. 2006; p. 2349.
8. Xiang QS, Ye FQ. Correction for geometric distortion and N/2 ghosting in EPI by phase labeling for additional coordinate encoding (PLACE). *Magn Reson Med* 2007;57:731–741.
9. Hoge WS, Tan H, Kraft RA. Robust EPI Nyquist ghost elimination via spatial and temporal encoding. *Magn Reson Med* 2010;64:1781–1791.
10. Xu D, King KF, Zur Y, Hinks RS. Robust 2D phase correction for echo planar imaging under a tight field-of-view. *Magn Reson Med* 2010;64:1800–1813.
11. Hoge WS, Polimeni JR. Dual-polarity GRAPPA for simultaneous reconstruction and ghost correction of echo planar imaging data. *Magn Reson Med* 2016;76:32–44.
12. Chang HC, Chen NK. Joint correction of Nyquist artifact and minuscule motion-induced aliasing artifact in interleaved diffusion weighted EPI data using a composite two-dimensional phase correction procedure. *Magn Reson Imag* 2016;34:974–979.
13. Yarach U, In MH, Chatnuntawech I, Bilgic B, Godenschweger F, Mattern H, Sciarra A, Speck O. Model-based iterative reconstruction for single-shot EPI at 7T. *Magn Reson Med* 2017;78:2250–2264.
14. Ianni JD, Welch EB, Grissom WA. Ghost reduction in echo-planar imaging by joint reconstruction of images and line-to-line delays and phase errors. *Magn Reson Med* 2018;79:3114–3121.
15. Xie VB, Lyu M, Liu Y, Feng Y, Wu EX. Robust EPI Nyquist ghost removal by incorporating phase error correction with sensitivity encoding (PEC-SENSE). *Magn Reson Med* 2018;79:943–951.
16. Lee J, Jin KH, Ye JC. Reference-free EPI Nyquist ghost correction using annihilating filter-based low rank Hankel matrix for K-space interpolation. *Magn Reson Med* 2016;76:1775–1789.

17. Mani M, Jacob M, Kelley D, Magnotta V. Multi-shot sensitivity-encoded diffusion data recovery using structured low-rank matrix completion (MUSSELS). *Magn Reson Med* 2017;78:494–507.
18. Lobos RA, Kim TH, Hoge WS, Haldar JP. Navigator-free EPI ghost correction with structured low-rank matrix models: New theory and methods. *IEEE Trans Med Imag* 2018;37:2390–2402.
19. Lyu M, Barth M, Xie VB, Liu Y, Ma X, Feng Y, Wu EX. Robust SENSE reconstruction of simultaneous multislice EPI with low-rank enhanced coil sensitivity calibration and slice-dependent 2D Nyquist ghost correction. *Magn Reson Med* 2018;80:1376–1390.
20. Liu Y, Lyu M, Barth M, Yi Z, Leong AT, Chen F, Feng Y, Wu EX. PEC-GRAPPA reconstruction of simultaneous multislice EPI with slice-dependent 2D Nyquist ghost correction. *Magn Reson Med* 2019;81:1924–1934.
21. Haldar JP. Autocalibrated LORAKS for fast constrained MRI reconstruction. In: *Proc. IEEE Int. Symp. Biomed. Imag.*.. 2015; pp. 910–913.
22. Griswold MA, Jakob PM, Heidemann RM, Nittka M, Jellus V, Wang J, Kiefer B, Haase A. Generalized autocalibrating partially parallel acquisitions (GRAPPA). *Magn Reson Med* 2002;47:1202–1210.
23. Lustig M, Pauly JM. SPIRiT: Iterative self-consistent parallel imaging reconstruction from arbitrary  $k$ -space. *Magn Reson Med* 2010;65:457–471.
24. Zhang J, Liu C, Moseley ME. Parallel reconstruction using null operations. *Magn Reson Med* 2011;66:1241–1253.
25. Bilgic B, Kim TH, Liao C, Manhard MK, Wald LL, Haldar JP, Setsompop K. Improving parallel imaging by jointly reconstructing multi-contrast data. *Magn Reson Med* 2018; 80:619–632.
26. Lobos RA, Javed A, Nayak KS, Hoge WS, Haldar JP. Robust autocalibrated LORAKS for EPI ghost correction. In: *Proc. IEEE Int. Symp. Biomed. Imag.*.. 2018; pp. 663–666.

27. Lobos RA, Javed A, Nayak KS, Hoge WS, Haldar JP. Robust autocalibrated LORAKS for improved EPI ghost correction with structured low-rank matrix models. In: *Proc. Int. Soc. Magn. Reson. Med.*. 2018; p. 3533.
28. Liang ZP, Haacke EM, Thomas CW. High-resolution inversion of finite Fourier transform data through a localised polynomial approximation. *Inverse Probl* 1989;5:831–847.
29. Uecker M, Lai P, Murphy MJ, Virtue P, Elad M, Pauly JM, Vasanawala SS, Lustig M. ESPIRiT – an eigenvalue approach to autocalibrating parallel MRI: Where SENSE meets GRAPPA. *Magn Reson Med* 2014;71:990–1001.
30. Shin PJ, Larson PEZ, Ohliger MA, Elad M, Pauly JM, Vigneron DB, Lustig M. Calibrationless parallel imaging reconstruction based on structured low-rank matrix completion. *Magn Reson Med* 2014;72:959–970.
31. Haldar JP. Low-Rank Modeling of Local-Space Neighborhoods (LORAKS) for Constrained MRI. *IEEE Trans Med Imag* 2014;33:668–681.
32. Haldar JP, Zhuo J. P-LORAKS: Low-rank modeling of local k-space neighborhoods with parallel imaging data. *Magn Reson Med* 2015;75:1499–1514.
33. Ongie G, Jacob M. Off-the-grid recovery of piecewise constant images from few Fourier samples. *SIAM J Imaging Sci* 2016;9:1004–1041.
34. Jin KH, Lee D, Ye JC. A general framework for compressed sensing and parallel MRI using annihilating filter based low-rank Hankel matrix. *IEEE Trans Comput Imaging* 2016;2:480–495.
35. Haldar JP, Setsompop K. Linear predictability in MRI reconstruction: Leveraging shift-invariant Fourier structure for faster and better imaging. arXiv preprint arXiv:190303141 2019;.
36. Pruessmann KP, Weiger M, Scheidegger MB, Boesiger P. SENSE: Sensitivity encoding for fast MRI. *Magn Reson Med* 1999;42:952–962.

37. Kim TH, Haldar JP. LORAKS software version 2.0: Faster implementation and enhanced capabilities. Technical Report USC-SIPI-443. University of Southern California. Los Angeles, CA. 2018.
38. Ongie G, Jacob M. A fast algorithm for convolutional structured low-rank matrix recovery. *IEEE Trans Comput Imaging* 2017;3:535–550.
39. Reeder SB, Atalar E, Faranesh AZ, McVeigh ER. Referenceless interleaved echo-planar imaging. *Magn Reson Med* 1999;41:87–94.
40. Grieve SM, Blamire AM, Styles P. Elimination of Nyquist ghosting caused by read-out to phase-encode gradient cross-terms in EPI. *Magn Reson Med* 2002;47:337–343.
41. Chen NK, Avram AV, Song AW. Two-dimensional phase cycled reconstruction for inherent correction of echo-planar imaging Nyquist artifacts. *Magn Reson Med* 2011;66:1057–1066.
42. Javed A, Jao T, Nayak KS. Velocity sensitivity of inner-volume echo-planar imaging. In: *Proc. SCMR*. 2018; p. 334.
43. Buehrer M, Boesiger P, Kozerke S. Virtual body coil calibration for phased-array imaging. In: *Proc. Int. Soc. Magn. Reson. Med.*. 2009; p. 760.
44. Kim TH, Haldar JP. The Fourier radial error spectrum plot: A more nuanced quantitative evaluation of image reconstruction quality. In: *Proc. IEEE Int. Symp. Biomed. Imag.*. 2018; pp. 61–64.
45. Mani M, Jacob M, McKinnon G, Yang B, Rutt B, Kerr A, Magnotta V. SMS-MUSSELS: A navigator-free reconstruction for slice-accelerated multi-shot diffusion imaging. In: *Proc. Int. Soc. Magn. Reson. Med.*. 2019; p. 0233.
46. Bilgic B, Liao C, Manhard MK, Tian Q, Chatnuntawech I, Iyer SS, Cauley SF, Feiweier T, Giri S, Y Hu aYH, Polimeni JR, Wald LL, Setsompop K. Robust high-quality multi-shot EPI with low-rank prior and machine learning. In: *Proc. Int. Soc. Magn. Reson. Med.*. 2019; p. 1250.

## FIGURE AND TABLE CAPTIONS

**Figure 1:** ACS data and reconstruction results for in vivo gradient-echo brain data with an axial slice orientation for different parallel imaging acceleration factors. Note that the first four acceleration factors ( $R = 1-4$ ) were acquired from one subject during a single scan session while the last two acceleration factors ( $R = 5, 6$ ) were acquired from a different subject on a different day, which explains the visual discontinuity between these cases.

**Figure 2:** tSNR maps for DPG and RAC-LORAKS from  $R = 2$  gradient-echo brain data with an axial slice orientation.

**Figure 3:** ACS data and reconstruction results for in vivo gradient-echo brain data with a double-oblique slice orientation for different parallel imaging acceleration factors. For reference, we also show the interpolarity phase difference as estimated from a coil-combined RAC-LORAKS result. These phase images have been masked to suppress background noise and windowed (black =  $0.01\pi$  radians, white =  $0.2\pi$  radians) to highlight the relevant phase structure. As can be seen, complicated 2D nonlinear phase differences are present in many of these cases.

**Figure 4:** Reconstruction results for multi-channel simulated data with different parallel imaging acceleration factors.

**Figure 5:** ESPs for the multi-channel simulation results shown in Fig. 4. The vertical axis of each ESP uses a consistent range to enable comparisons between different acceleration factors.

**Figure 6:** Reconstruction results for single-channel simulated data with different acceleration factors.

**Figure 7:** ACS data and reconstruction results for three representative slices from in vivo diffusion brain data ( $R = 3$ ). Each row corresponds to a different slice.

**Figure 8:** The same results shown in Fig. 7, but with  $10\times$  intensity amplification to better highlight the ghosting characteristics.

**Figure 9:** ACS data and reconstruction results for unaccelerated in vivo cardiac data. The two rows show the same results, but the second row has  $10\times$  intensity amplification to better highlight the ghosting characteristics.

**Table 1:** NRMSEs for the multi-channel simulation results shown in Fig. 4. For each acceleration factor, the smallest values are highlighted in bold.

**Supporting Information Figure S1:** Illustration of EPI ghost correction. The top row of this figure shows EPI images obtained from different methods, while the bottom row shows the same images with  $10\times$  intensity amplification to highlight the ghost characteristics. If EPI data is naively reconstructed without accounting for the systematic differences between data acquired with positive and negative readout gradient polarities (“Uncorrected”), then strong Nyquist ghosts appear in the image as indicated with arrows. Modern EPI techniques frequently try to eliminate these artifacts using navigator information to estimate the systematic differences between the data collected with different readout polarities. In the navigator-based example we show (“Navigator”), the navigator information was collected using a 3-line EPI acquisition with the phase encoding gradients turned off, and the difference between positive and negative gradient polarities was modeled using constant and 1D linear phase terms. Although this approach substantially reduces Nyquist ghosts, it is common for some amount of residual ghosting to still be present in the images, particularly in cases where simple 1D phase modeling is inadequate to capture the differences between the two gradient polarities. We also show an example of our proposed approach (“RAC-LORAKS”), which can account for more complicated variations between the different gradient polarities, and which is substantially more successful at suppressing Nyquist ghosts in this example.

**Supporting Information Figure S2:** Illustration of the EPI and ACS datasets used in simulation. The top row shows coil-combined multi-channel data, while the bottom row shows representative single-channel images. We also show the interpolarity phase difference for the coil-combined ACS data (for visualization, this phase image has been masked and windowed such that black =  $0.1\pi$  radians and white =  $0.6\pi$  radians), as well as the difference in the interpolarity phase difference between the coil-combined EPI and ACS data (for visualization, this phase image has been masked and windowed such that black =  $0.01\pi$  radians and white =  $0.05\pi$  radians).

**Supporting Information Table S1:** NRMSEs for the single-channel simulation results shown in Fig. 6. For each acceleration factor, the smallest values are highlighted in bold.

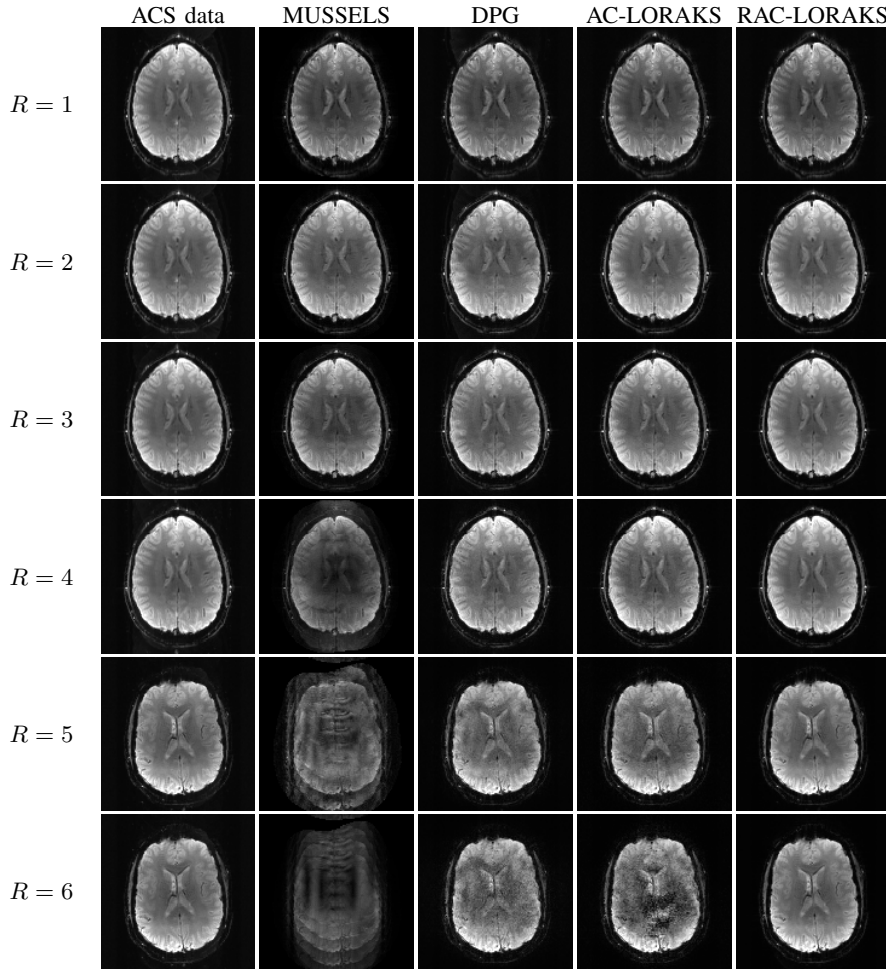


Figure 1: ACS data and reconstruction results for in vivo gradient-echo brain data with an axial slice orientation for different parallel imaging acceleration factors. Note that the first four acceleration factors ( $R = 1-4$ ) were acquired from one subject during a single scan session while the last two acceleration factors ( $R = 5, 6$ ) were acquired from a different subject on a different day, which explains the visual discontinuity between these cases.

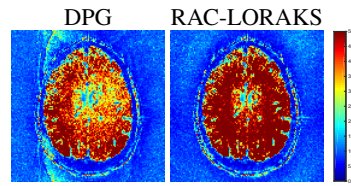


Figure 2: tSNR maps for DPG and RAC-LORAKS from  $R = 2$  gradient-echo brain data with an axial slice orientation.

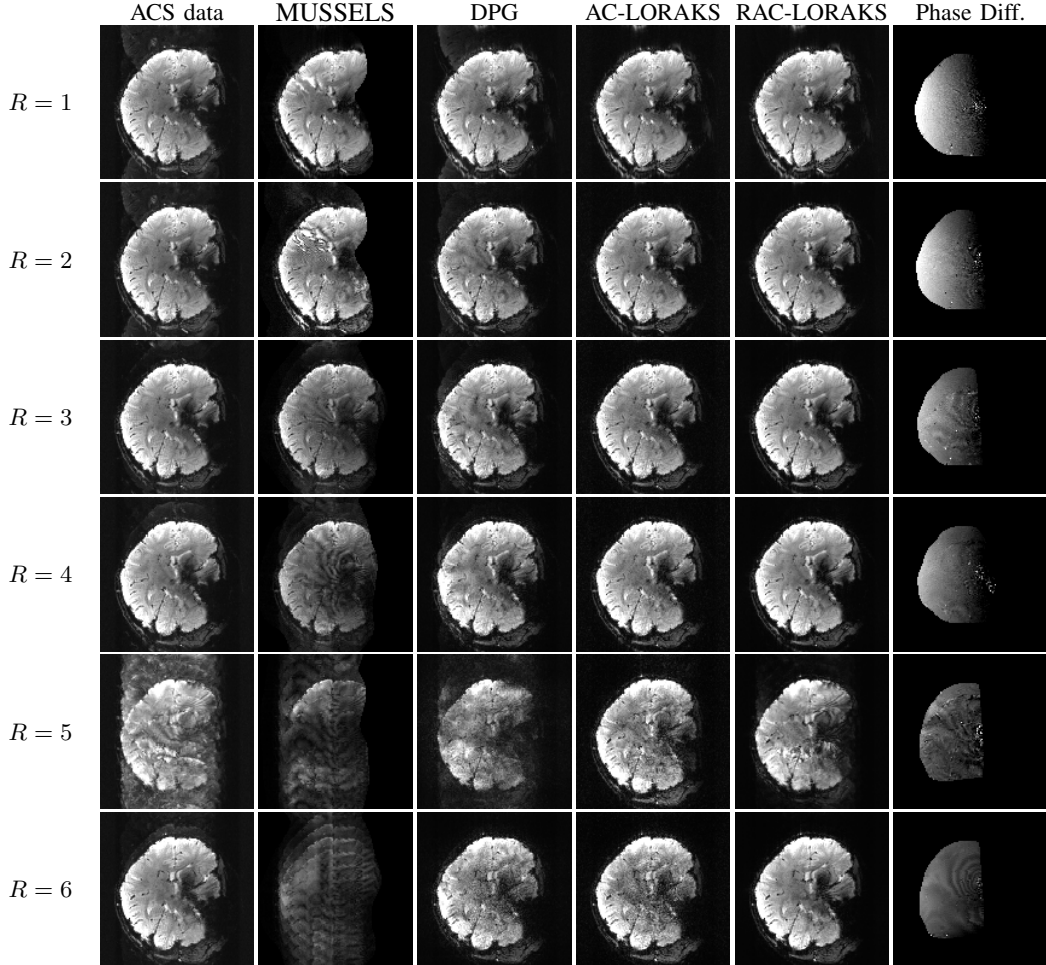


Figure 3: ACS data and reconstruction results for in vivo gradient-echo brain data with a double-oblique slice orientation for different parallel imaging acceleration factors. For reference, we also show the interpolarity phase difference as estimated from a coil-combined RAC-LORAKS result. These phase images have been masked to suppress background noise and windowed (black =  $0.01\pi$  radians, white =  $0.2\pi$  radians) to highlight the relevant phase structure. As can be seen, complicated 2D nonlinear phase differences are present in many of these cases.

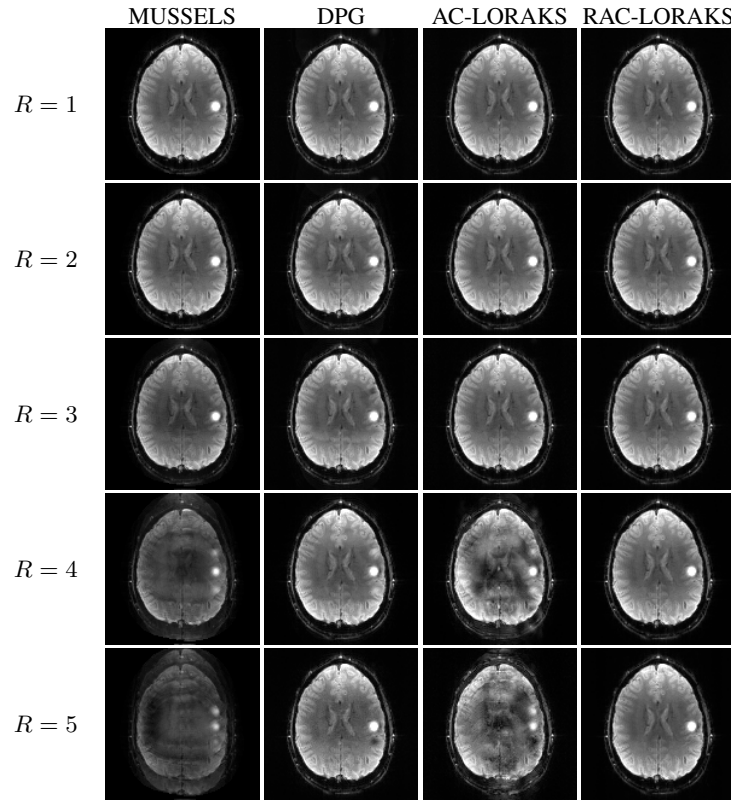


Figure 4: Reconstruction results for multi-channel simulated data with different parallel imaging acceleration factors.

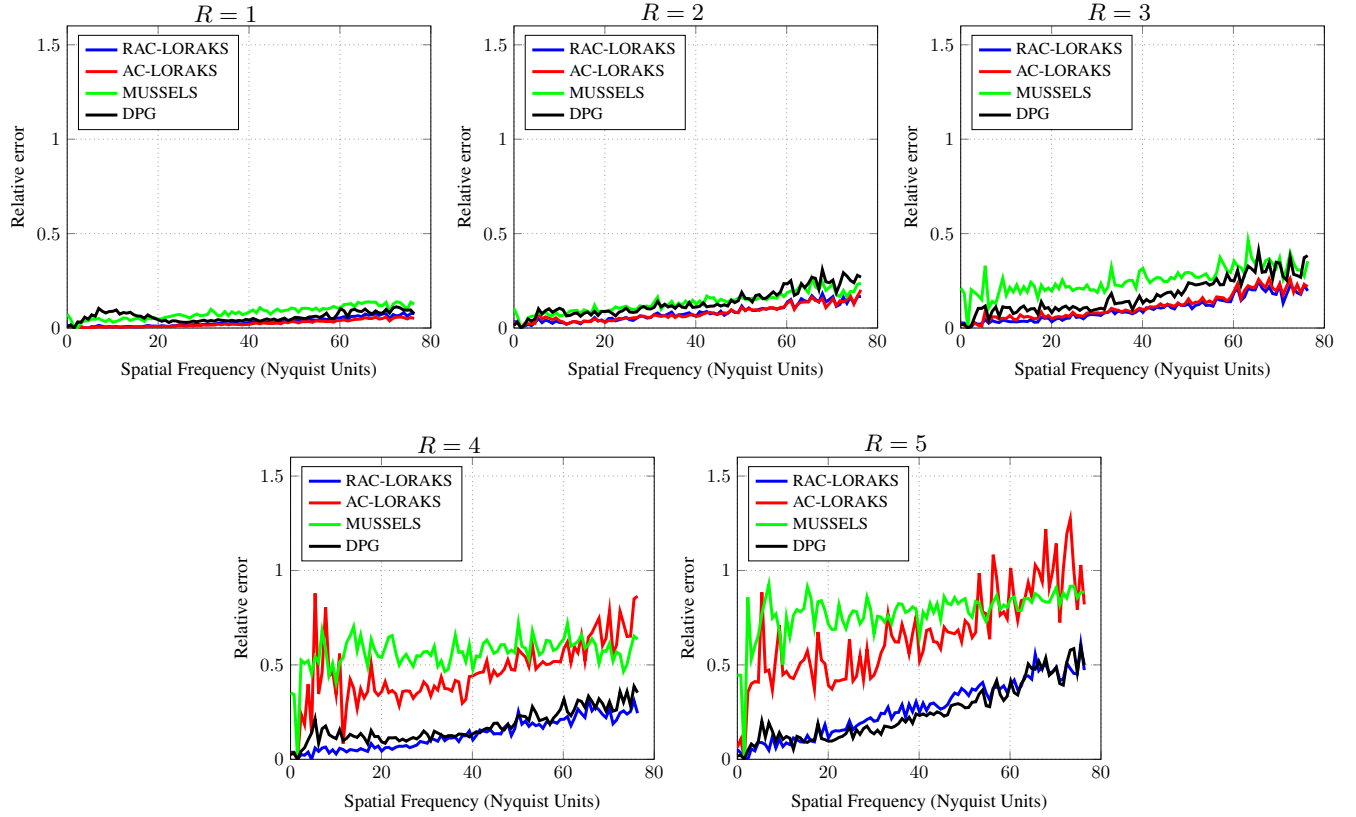


Figure 5: ESPs for the multi-channel simulation results shown in Fig. 4. The vertical axis of each ESP uses a consistent range to enable comparisons between different acceleration factors.

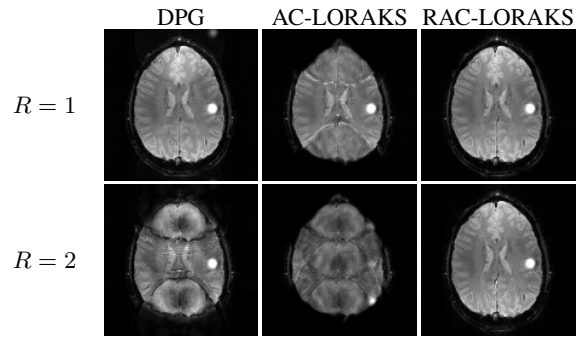


Figure 6: Reconstruction results for single-channel simulated data with different acceleration factors.

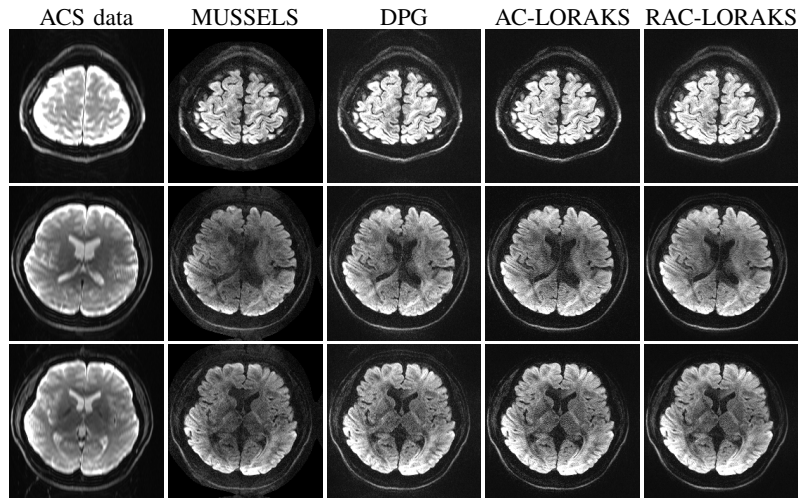


Figure 7: ACS data and reconstruction results for three representative slices from *in vivo* diffusion brain data ( $R = 3$ ). Each row corresponds to a different slice.

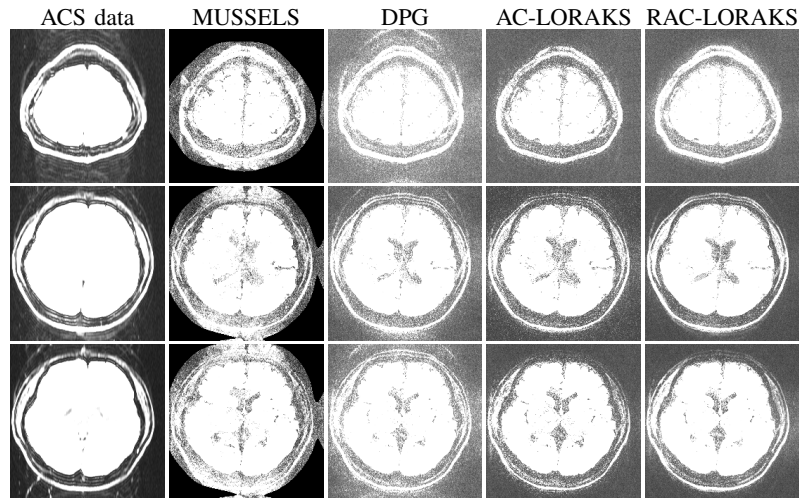


Figure 8: The same results shown in Fig. 7, but with  $10\times$  intensity amplification to better highlight the ghosting characteristics.

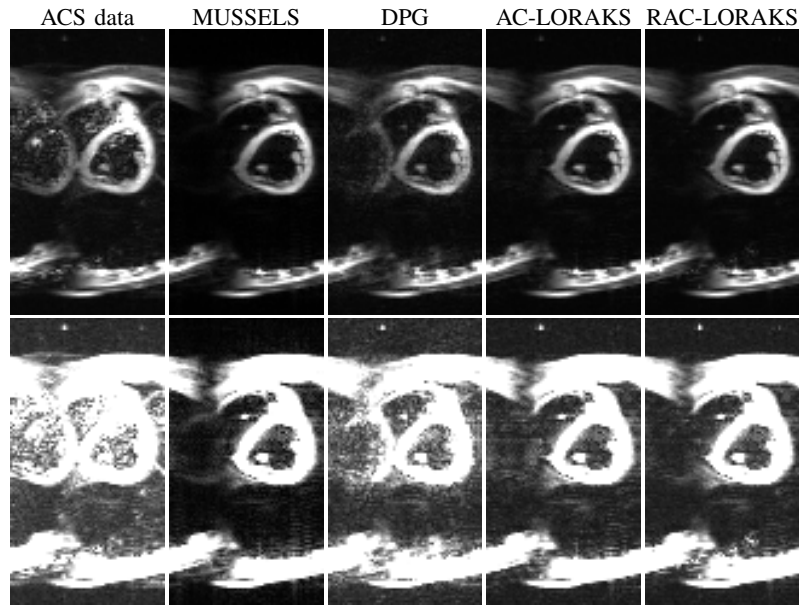
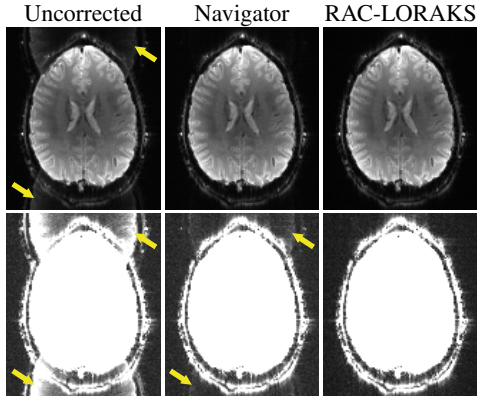


Figure 9: ACS data and reconstruction results for unaccelerated *in vivo* cardiac data. The two rows show the same results, but the second row has  $10\times$  intensity amplification to better highlight the ghosting characteristics.

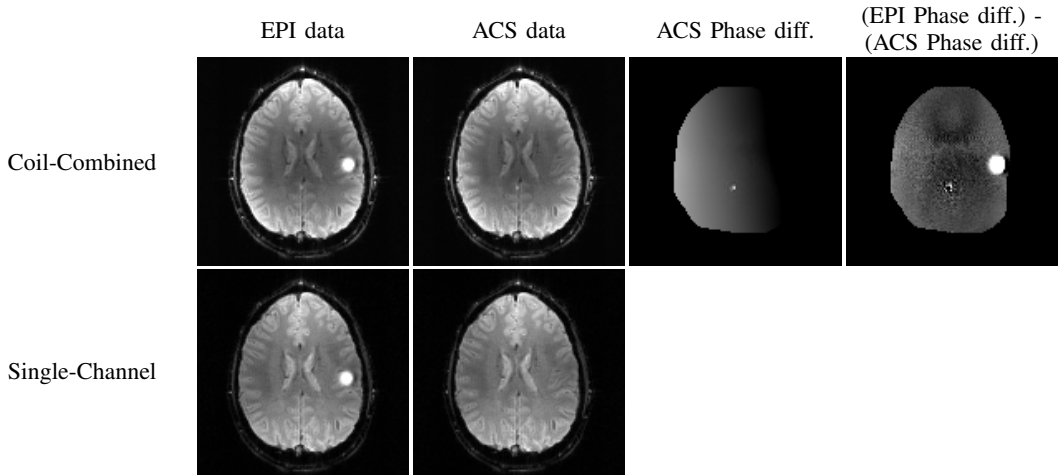
Table 1: NRMSEs for the multi-channel simulation results shown in Fig. 4. For each acceleration factor, the smallest values are highlighted in bold.

	MUSSELS	DPG	AC-LORAKS	RAC-LORAKS
$R = 1$	0.108	0.090	<b>0.056</b>	0.060
$R = 2$	0.127	0.103	0.087	<b>0.077</b>
$R = 3$	0.256	0.107	0.091	<b>0.080</b>
$R = 4$	0.568	0.111	0.464	<b>0.085</b>
$R = 5$	0.731	<b>0.121</b>	0.531	0.123

## SUPPORTING INFORMATION



Supporting Information Figure S1: Illustration of EPI ghost correction. The top row of this figure shows EPI images obtained from different methods, while the bottom row shows the same images with 10 $\times$  intensity amplification to highlight the ghost characteristics. If EPI data is naively reconstructed without accounting for the systematic differences between data acquired with positive and negative readout gradient polarities (“Uncorrected”), then strong Nyquist ghosts appear in the image as indicated with arrows. Modern EPI techniques frequently try to eliminate these artifacts using navigator information to estimate the systematic differences between the data collected with different readout polarities. In the navigator-based example we show (“Navigator”), the navigator information was collected using a 3-line EPI acquisition with the phase encoding gradients turned off, and the difference between positive and negative gradient polarities was modeled using constant and 1D linear phase terms. Although this approach substantially reduces Nyquist ghosts, it is common for some amount of residual ghosting to still be present in the images, particularly in cases where simple 1D phase modeling is inadequate to capture the differences between the two gradient polarities. We also show an example of our proposed approach (“RAC-LORAKS”), which can account for more complicated variations between the different gradient polarities, and which is substantially more successful at suppressing Nyquist ghosts in this example.



Supporting Information Figure S2: Illustration of the EPI and ACS datasets used in simulation. The top row shows coil-combined multi-channel data, while the bottom row shows representative single-channel images. We also show the interpolarity phase difference for the coil-combined ACS data (for visualization, this phase image has been masked and windowed such that black =  $0.1\pi$  radians and white =  $0.6\pi$  radians), as well as the difference in the interpolarity phase difference between the coil-combined EPI and ACS data (for visualization, this phase image has been masked and windowed such that black =  $0.01\pi$  radians and white =  $0.05\pi$  radians).

Supporting Information Table S1: NRMSEs for the single-channel simulation results shown in Fig. 6. For each acceleration factor, the smallest values are highlighted in bold.

	<b>DPG</b>	<b>AC-LORAKS</b>	<b>RAC-LORAKS</b>
$R = 1$	0.132	0.572	<b>0.036</b>
$R = 2$	0.531	0.795	<b>0.133</b>